nature communications

Article

https://doi.org/10.1038/s41467-025-65987-3

Stable and efficient PbS quantum dot photoelectrodes enable photoelectrochemical hydrogen production without sacrificial agents

Received: 17 September 2024

Accepted: 27 October 2025

Published online: 11 December 2025

Check for updates

Hwa-Young Yang[1,2,5], Muhibullah Al Mubarok[1,5], Sarang Kim[1,5], Su-Ho Lee[1,5], Je Min Yu[1], Jaewon Jo[1], Ahmad Tayyebi[1], Sung-Yeon Jang[1,3] ✉ & Ji-Wook Jang[1,3,4] ✉

Chalcogenides are promising materials for photoelectrochemical (PEC) water splitting owing to their suitable band gaps, favourable band alignments, and efficient charge transport properties. However, their practical application has been limited by poor stability in aqueous environments, as they are prone to self-oxidation prior to water oxidation. This instability typically necessitates the use of sacrificial agents to scavenge photogenerated holes, thereby restricting long-term device operation and real-world implementation. Here we report a metal-encapsulated PbS quantum dot (PbS-QD) solar cell-based photoelectrode that simultaneously achieves high photocurrent and long-term operational stability for PEC water splitting without sacrificial agents. The optimised PbS-QD-based photoanode delivers a photocurrent density of 18.6 mA cm^{-2} at 1.23 V versus the reversible hydrogen electrode in 1.0 M NaOH, retaining 90% of its initial performance over 24 h. These values are comparable to those reported for chalcogenide-based photoelectrodes operating in the presence of sacrificial agents.

Photoelectrochemical (PEC) water splitting has garnered significant attention as a method for solar hydrogen (H_2) production since Honda and Fujishima first demonstrated this approach using a TiO_2 photoelectrode in 1972[1–5]. Over the past five decades, a variety of PEC water-splitting systems have been developed using metal oxides such as WO_3, $BiVO_4$, α-Fe_2O_3, $CuWO_4$, and Bi_2WO_6, which are favoured for their intrinsic stability in aqueous environments[6–9]. However, these metal oxide-based photocatalysts are limited by their low photocurrent density (J_{ph} < 7 mA cm^{-2} at 1.23 V vs. reversible hydrogen electrode (RHE)). This level remains insufficient for practical applications, as PEC water-splitting technology requires a minimum J_{ph} of 8.1 mA cm^{-2} to achieve a solar-to-hydrogen (STH) conversion efficiency of 10%. The limited performance primarily arises from the wide bandgaps, unfavourable conduction and valence band positions, and poor charge transport properties inherent to metal oxide photoelectrodes[10–13].

Chalcogenide-based materials such as CdS, CdSe, and PbS have attracted significant attention due to their suitable bandgaps and band positions for PEC water splitting, as well as their favourable charge transport properties[14–17]. These chalcogenide-based photoelectrodes have demonstrated higher J_{ph} compared to conventional metal oxide-

[1]School of Energy and Chemical Engineering, Ulsan National Institute of Science and Technology, Ulsan, Republic of Korea. [2]Center for Wave Energy Materials, Ulsan National Institute of Science and Technology, Ulsan, Republic of Korea. [3]Graduate School of Carbon Neutrality, Ulsan National Institute of Science and Technology, Ulsan, Republic of Korea. [4]Emergent Hydrogen Technology R&D Centre, Ulsan National Institute of Science and Technology, Ulsan, Republic of Korea. [5]These authors contributed equally: Hwa-Young Yang, Muhibullah Al Mubarok, Sarang Kim, Su-Ho Lee.
✉e-mail: syjang@unist.ac.kr; jiwjang@unist.ac.kr

based photoelectrodes. For example, a CdS/Ti-Nb-O photoanode exhibited a J_{ph} of 16.11 mA cm^{-2} at 1.23 V vs. RHE[18], while IrO_x/CdS/CdSe and ZnS/CdS/PbS@CdS/TiO_2 photoanodes achieved 11.2 mA cm^{-2} and 13.9 mA cm^{-2} at 0.6 V vs. RHE, respectively[19,20]. Among these materials, PbS has drawn particular attention due to its strong light absorption and high quantum efficiency. Bulk PbS possesses a narrow bandgap (~0.41 eV), which is insufficient to drive PEC water splitting, as the reaction requires a thermodynamic potential of at least 1.23 V. To overcome this limitation, many studies have utilised the quantum confinement effect by reducing PbS to the nanoscale, thereby widening its bandgap to approximately 1.35 eV[21]. A thin p-type PbS quantum dot (QD; p-QD) layer was deposited as the hole-transport layer between the n-type PbS-QD (n-QD) photoactive layer and the anode. This configuration provides favourable band alignment to enhance hole extraction and block undesired electron flow, thereby reducing surface recombination and improving photocurrent collection efficiency[22]. As a result, PbS-QD have been extensively investigated for PEC applications. To further enhance performance, PbS-QD are often integrated with wide-band-gap semiconductors such as TiO_2 and $BiVO_4$, forming PbS-QD-based photoelectrodes that broaden light absorption and improve charge separation.

Despite recent advancements, many PEC systems still require a continuous supply of sacrificial agents such as S^{2-}/SO_3^{2-} to maintain operational stability. This dependence substantially increases running costs, as an equimolar quantity of costly reagents is consumed per mole of H_2 produced, ultimately undermining the overall economic viability of the process[23–30]. Although the theoretical J_{ph} of quantum-confined PbS is estimated to be ~30 mA cm^{-2}, the practical performance remains far below this limit due to intrinsic instability and severe surface recombination[21].

Herein, we report the development of a stable chalcogenide-based PEC system that operates without the need for a sacrificial agent. This is achieved by employing metal foil-encapsulated PbS-QD-based photoanodes. The stability of PbS-QD against photocorrosion was enhanced by preventing electrolyte penetration using a Ni metal foil in combination with Field's metal (FM). FM was selected for its good wettability and ability to form a uniform, stable contact with both the PbS-QD layer and the Ni foil. Additionally, the metallic nature of FM ensures high conductivity, facilitating the efficient transfer of photogenerated holes from the PbS-QD layer to the Ni foil. The Ni foil further acts as an efficient catalyst for the oxygen evolution reaction, thereby contributing to the improved overall performance of the device. The Ni/FM-encapsulated PbS-QD (Ni/FM/PbS-QD) photoanodes achieved a J_{ph} of 18.6 mA cm^{-2} at 1.23 V vs. RHE, demonstrating performance comparable to other chalcogenide materials operating with a sacrificial agent and competitive with representative metal oxide-based photoanodes. Additionally, they retained approximately 90% of their initial photocurrent over 24 h, whereas the unprotected photoanodes lost all activity within a few minutes. We further examined the key factors influencing chemical and photostability and explored strategies to enhance long-term durability.

Results

Characterisation of PbS-QD solar cell

A PbS-QD solution was synthesized via a modified hot-injection method, involving the rapid injection of precursors into a hot coordinating solvent[31]. The transmission electron microscopy (TEM) image in Fig. 1a shows the as-synthesized PbS-QD, with an average size of 2.7 ± 0.9 nm as determined from the size distribution histogram (Supplementary Fig. 1). X-ray diffraction (XRD) analysis confirmed that the diffraction peaks match those of face-centred cubic PbS, indicating that the crystal structure is retained even at the nanoscale (Fig. 1b). Subsequently, light-absorbing n-type PbS-QD ink (n-QD) was prepared via solution-phase ligand exchange of the as-synthesized PbS-QD with PbI_2 (Supplementary Fig. 2 and Supplementary Note 1)[32]. The ultraviolet-visible-near infrared (UV–vis–NIR) and photoluminescence

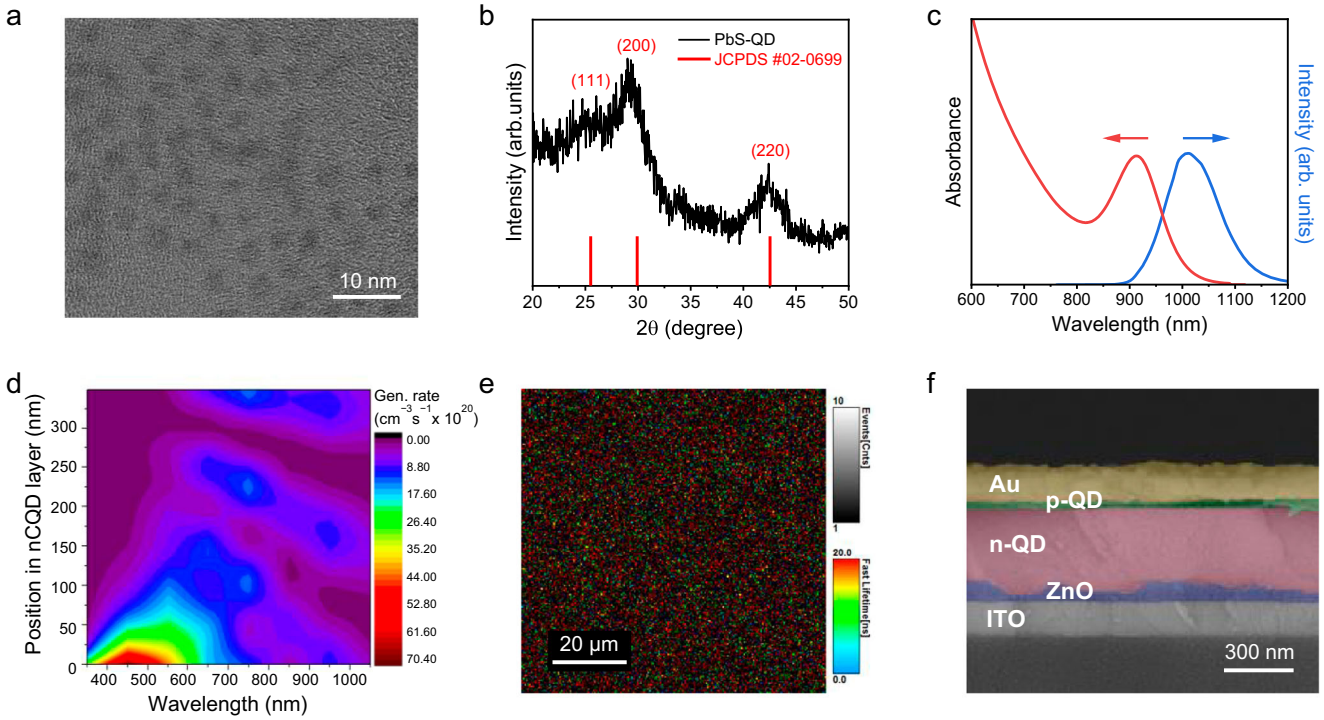

Fig. 1 | Characterisation of the PbS-QD solar cell. a Transmission electron microscopy (TEM) image of the as-synthesised PbS-QD. **b** X-ray diffraction (XRD) pattern of the n-QD layer. The standard diffraction pattern (JCPDS #02-0699) for bulk PbS is included as an inset. **c** Ultraviolet–visible–near-infrared (UV–vis–NIR) absorption and photoluminescence (PL) spectra of the n-QD layer (PL intensity is shown on the right y-axis in blue). **d** Charge generation rate map of the n-QD layer in the PbS-QD solar cell. **e** Fluorescence lifetime imaging microscopy (FLIM) image of the n-QD film. **f** Cross-sectional scanning electron microscopy (SEM) image of ITO/ZnO/n-QD/p-QD/Au device structure.

(PL) spectra of the n-QD film on a glass substrate are shown in Fig. 1c. The first excitonic absorption peak appears at ~920 nm, corresponding to a bandgap of 1.35 eV. The average size of the n-QD was estimated to be 3.01 nm using the optical bandgap method described by Hyun et al.[33], consistent with the TEM data considering size distribution. Additionally, application of Moreels' equations yielded a calculated diameter of 2.95 nm[34], further confirming the quantum confinement effect, as the bandgap is significantly larger than that of bulk PbS (0.41 eV). Figure 1d illustrates the spatial distribution of the charge generation rate within the n-QD layer, as determined by optical simulation. The transfer matrix formalism (TMF) method was employed using MATLAB code developed by the McGehee group. Optical constants for ITO, ZnO, n-QD, p-QD, and Au layers across the wavelength range of 400–1200 nm were obtained from previously reported experimental data[31]. The front region of the n-QD layer shows a high charge generation rate for light in the 400–700 nm range, while the rear region exhibits charge generation around 900 nm. This profile aligns well with the UV–vis–NIR spectrum of the n-QD layer, as shown in Fig. 1c and d. Additionally, the spatial distribution of lifetime decay characteristics in the n-QD light-absorbing layer on a glass substrate was assessed using fluorescence lifetime imaging microscopy (FLIM). The resulting lifetime decay map revealed a uniform distribution across an 80 μm × 80 μm area, confirming the homogeneity of the n-QD layer (Fig. 1e). The hole-transporting layer was composed of a thin p-QD layer, prepared via ligand exchange of the as-synthesized PbS-QD with 1,2-ethanedithiol (EDT) (Supplementary Fig. 2). Figure 1f presents a cross-sectional scanning electron microscopy (SEM) image of the PbS-QD solar cell. The measured thicknesses of the ZnO electron-transport layer, the n-QD photoactive layer, the p-QD hole-transport layer, and the Au electrode are 40 nm, 300 nm, 40 nm, and 70 nm, respectively. The n-QD layer, serving as the light absorber, was fabricated using a one-step spin-coating process, avoiding the conventional layer-by-layer deposition approach.

Photoelectrochemical performance of PbS-QD-based photoanodes

To evaluate the photoelectrochemical (PEC) performance of the PbS-QD-based photoanodes, we employed a three-electrode system consisting of a working electrode, a saturated Hg/HgO reference electrode, and a Pt mesh counter electrode. The PEC tests were conducted under one-sun illumination (AM 1.5 G, 100 mW cm^{-2}) using a UV cut-off filter ($\lambda \geq 420$ nm) to provide visible-light illumination. As shown in Fig. 2a, the bare PbS-QD photoanode exhibited poor PEC performance. To enhance its performance, we investigated suitable encapsulation and passivation strategies and selected Ni as the encapsulating material for the fabrication of the PbS-QD-based photoanode. In alkaline solution, its surface transforms into nickel hydroxide, which serves as an efficient electrocatalyst for the oxygen evolution reaction (OER)[35–37]. To achieve uniform film quality, we employed two approaches: Ni sputter coating and Ni foil physical adhesion. First, we used Ni sputtering, as sputtering metal onto the photoelectrode is a straightforward and widely used technique to enhance the stability of the photoelectrode (denoted as Spu-Ni/PbS-QD). In Fig. 2a, the Spu-Ni/PbS-QD photoanode exhibited a significantly higher J_{ph} compared to the bare PbS-QD photoanode. However, the Spu-Ni/PbS-QD photoanode still exhibited poor stability, with complete degradation observed within just 20 min (Fig. 2b and Supplementary Fig. 3; magnified photocurrent–time (J_{ph}–t) curves). To further assess its durability, sequential linear sweep voltammetry (LSV) scans were performed, revealing rapid performance degradation within just three cycles, in contrast to the more stable Ni/FM/PbS-QD photoanode (Supplementary Fig. 4). We also examined whether the sputtered Ni layer could protect the PbS-QD surface from corrosion in the absence of sacrificial agents. To this end, UV–vis absorption spectra of the PbS-QD layer were recorded before and after immersion in 1.0 M NaOH. As shown in Supplementary Fig. 5, a reduction in absorbance across all wavelengths was observed after exposure, indicating that the sputtered Ni layer did not effectively shield the PbS-QD surface from chemical degradation. These results suggest that while sputtered Ni can act as a passivation layer and exhibit OER catalytic activity, it does not provide sufficient encapsulation to prevent electrolyte-induced corrosion of the PbS-QD layer in alkaline media. In contrast, when Ni foil physical adhesion with FM (denoted as Ni/FM/PbS-QD) was employed, the photoanode exhibited an onset potential of 0.85 V vs. RHE and a J_{ph} of 18.6 mA cm^{-2} at 1.23 V vs. RHE (Fig. 2b), demonstrating stable performance for 2 h without any noticeable degradation. To clarify the role of each layer in the photoanode architecture, we fabricated two control photoanodes: FM/PbS-QD, which includes only the FM layer without Ni foil, and Ni/PbS-QD, which includes only the Ni foil without the FM layer. The FM/PbS-QD photoanode exhibited a minimal photocurrent response, characterized by a high onset potential and an almost flat current–density profile, although the J_{ph} at high applied potential was slightly higher than that of the bare PbS-QD photoanode. This behaviour indicates poor charge transfer characteristics and sluggish OER kinetics. In contrast, the Ni/PbS-QD photoanode demonstrated only electrocatalytic activity at high applied potentials, suggesting that Ni alone does not significantly contribute to PEC performance enhancement. The LSV results highlight the distinct functional contributions of the Ni foil and FM layer: Ni promotes charge transfer from the PbS-QD layer to the electrolyte, while FM provides robust electronic and physical connectivity between the Au contact and the Ni foil, enabling effective device integration. Furthermore, in the Ni/FM/PbS-QD photoanode, FM —positioned between the Au layer and Ni foil—not only improves charge transfer but also serves as a protective barrier against ambient air and aqueous electrolytes.

To further support these findings, external quantum efficiency (EQE) and incident photon-to-current efficiency (IPCE) measurements were conducted to disentangle the effects of light absorption, charge generation, and interfacial charge transfer (Supplementary Fig. 6). Under nitrogen-purged conditions in a glove box, the EQE spectra of bare PbS-QD, FM/PbS-QD, and Ni/FM/PbS-QD photoanodes were nearly identical, indicating comparable optical absorption and photocarrier generation. Under operational conditions in 1.0 M NaOH, however, the IPCE responses diverged significantly. The bare PbS-QD exhibited substantially lower IPCE despite similar EQE, consistent with poor stability and rapid photocorrosion in alkaline electrolyte. In contrast, FM/PbS-QD and Ni/FM/PbS-QD maintained similarly high IPCE values, indicating that the FM interlayer affords a stable, conductive interface for efficient charge extraction. However, the Ni/PbS-QD photoanode displayed negligible EQE and IPCE, reflecting severe interfacial charge-transfer barriers arising from direct contact between Ni and PbS-QD. Although FM/PbS-QD and Ni/FM/PbS-QD showed comparable EQE and IPCE, only the Ni/FM/PbS-QD photoanode delivered a substantially higher J_{ph} in LSV (Fig. 2a), confirming the catalytic role of Ni in oxygen evolution. Collectively, these results attribute the ~20-fold J_{ph} enhancement to the synergistic effects of FM and Ni layers in improving stability, interfacial charge transfer, and catalytic activity, rather than to differences in light absorption or photogeneration.

The enhanced interfacial charge transport behaviour was further corroborated by electrochemical impedance spectroscopy (EIS) and intensity-modulated photocurrent spectroscopy (IMPS) analyses, as shown in Fig. 3 and Supplementary Fig. 7. EIS measurements were conducted over a potential range of 1.0–1.8 V vs. RHE. The Nyquist plots for the FM/PbS-QD, Ni/PbS-QD, and Ni/FM/PbS-QD photoanodes are presented in Fig. 3a–c. The arc radius in the fitted curves is proportional to the charge-transfer impedance; the Ni/FM/PbS-QD photoanode exhibits smaller arc radii than the other configurations, indicating reduced overall charge-transfer resistance. To gain further insight, resistance (R) and capacitance (C) parameters were extracted

https://doi.org/10.1038/s41467-025-65987-3

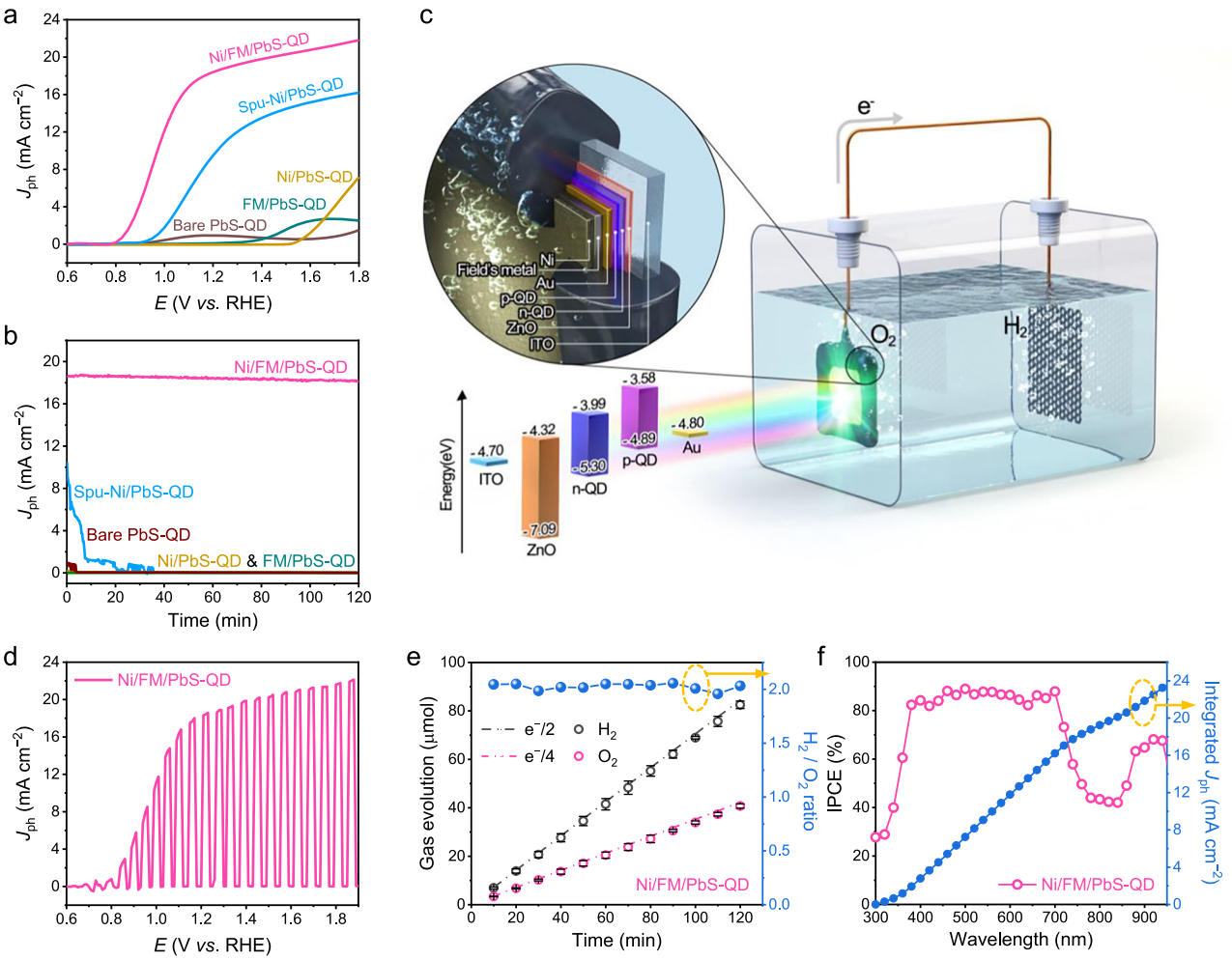

Fig. 2 | Photoelectrochemical (PEC) performance of PbS-QD-based photoanodes. a Linear sweep voltammetry (LSV) curves recorded at a scan rate of 5 mV s^{-1}. **b** photocurrent density–time (J_{ph}–t) curves for the as-prepared PbS-QD-based photoanodes under visible-light illumination (λ ≥ 420 nm). **c** Schematic illustration of the Ni/FM/PbS-QD photoanode used in the PEC water splitting system. **d** LSV curve of the Ni/FM/PbS-QD photoanode under chopped visible-light illumination (λ ≥ 420 nm). **e** Time-resolved H_2 and O_2 production, with the corresponding H_2/O_2 molar ratio indicated by the yellow arrow (right y-axis, blue), from the Ni/FM/PbS-QD photoanode under visible-light illumination (λ ≥ 420 nm). Error bars represent the standard deviation from five independent measurements. **f** Incident photon-to-current efficiency (IPCE) spectrum of the Ni/FM/PbS-QD photoanode recorded under monochromatic light illumination (300–950 nm), together with the corresponding integrated J_{ph}, indicated by the yellow arrow (right y axis, blue).

from the EIS data using a simplified equivalent circuit model (Fig. 3d). The Nyquist plots can be interpreted using three key elements in the equivalent circuit: R_s represents the series resistance, including the sheet resistance of the FTO substrate; the high-frequency arc corresponds to the charge-transfer resistance (R_{tr}) and chemical capacitance (C_{tr}), associated with photogenerated carrier transport within the multilayered photoanode; and the low-frequency arc reflects the recombination resistance (R_{rec}) and chemical capacitance (C_{rec}), related to radical-mediated PEC reactions within the electrical double layer. As shown in Fig. 3e, R_s exhibited no significant difference among the photoanodes. In Fig. 3f, h, both R_{tr} and R_{rec} decreased with increasing applied potential for all photoanodes, reflecting enhanced charge transport and suppressed side reactions at higher applied potential. However, the Ni/FM/PbS-QD photoanode exhibited significantly lower R_{tr} and R_{rec} values compared to the other photoanodes. The sharp decrease in R_{tr} highlights the improved interfacial contact and more efficient charge transfer between the PbS-QD layer and the Ni foil, confirming that the FM interlayer promotes electronic connectivity and facilitates charge transport. Additionally, the capacitance values C_{tr} and C_{rec} were notably higher in the Ni/FM/PbS-QD photoanode (Fig. 3g, i), suggesting a higher charge-carrier density that contributes to improved charge separation and reduced recombination. These effects collectively enhance PEC performance. In contrast, the FM/PbS-QD photoanode, which lacks the Ni foil, showed high R_{rec} and low C_{rec} values, indicating sluggish OER kinetics due to the absence of an efficient OER catalyst. To further investigate the role of the FM interlayer and Ni foil in interfacial charge transport, IMPS was performed. IMPS is a powerful technique for probing charge transfer and recombination dynamics at the semiconductor/electrolyte interface. As shown in Supplementary Fig. 7, electron transport time (τ_d), calculated from the low-frequency response of the IMPS plots, was shortest for the Ni/FM/PbS-QD photoanode across the entire potential range. This indicates efficient charge extraction and suppressed interfacial recombination, further confirming the beneficial role of the FM interlayer in facilitating charge transport. In contrast, the FM/PbS-QD photoanode showed minimal change with increasing applied potential, with consistently long τ_d values, reflecting poor charge-transfer kinetics and recombination-dominated behaviour due to the absence of an OER catalyst. The Ni/PbS-QD photoanode exhibited improved performance only at potentials above 1.6 V vs. RHE, likely due to the onset of electrocatalytic OER at the Ni surface. These results highlight the dual role of the FM layer and Ni substrate in enabling

https://doi.org/10.1038/s41467-025-65987-3

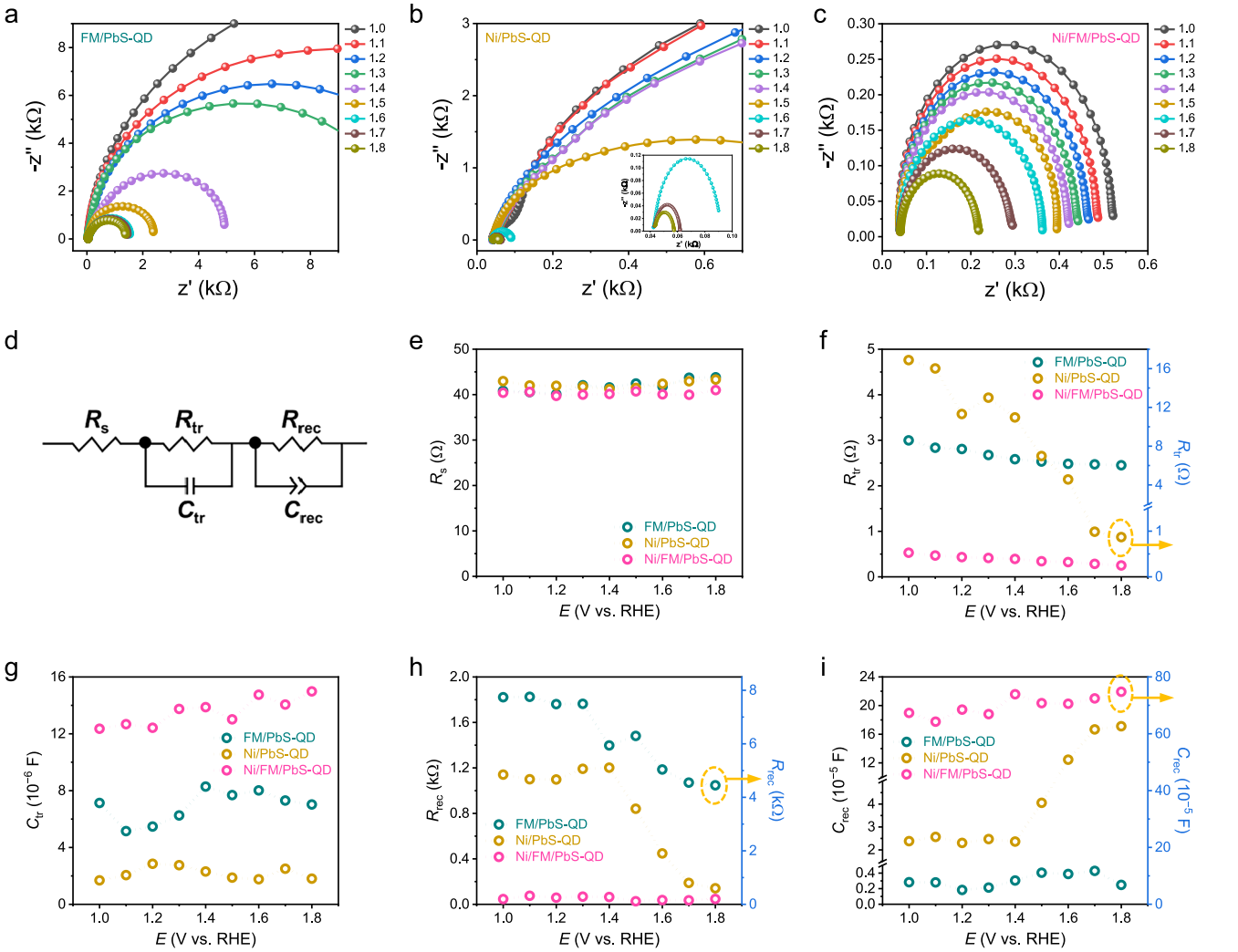

Fig. 3 | Electrochemical impedance spectroscopy (EIS) results of as-prepared PbS-QD-based photoanodes measured at various potentials under visible-light illumination (λ ≥ 420 nm). Nyquist plots of **a** FM/PbS-QD, **b** Ni/PbS-QD, and **c** Ni/FM/PbS-QD photoanodes. **d** Corresponding equivalent circuit model. **e** R_s represents the series resistance, including contributions from the ITO substrate, ionic conductivity of the electrolyte, and external contact resistance (e.g., wire connections). **f** The first high-frequency arc is associated with charge-transfer resistance (R_{tr}), with the value for Ni/PbS-QD indicated by the yellow arrow (right y-axis, blue) and **g** the corresponding chemical capacitance (C_{tr}). **h** The second low-frequency arc reflects recombination resistance (R_{rec}), with the FM/PbS-QD value indicated by the yellow arrow (right y-axis, blue) and **i** the chemical capacitance (C_{rec}), with the Ni/FM/PbS-QD value indicated by the yellow arrow (right y-axis, blue).

efficient charge transport and catalytic activity, thereby contributing to the enhanced PEC performance of the Ni/FM/PbS-QD photoanode. As shown in Fig. 2c, the PbS-QD-based photoanode was optimised with the structural configuration ITO/ZnO/n-QD/p-QD/Au/FM/Ni. Moreover, the Ni/FM/PbS-QD photoanode exhibited a stable and reproducible photoresponse under chopped light illumination (Fig. 2d). In Fig. 2e, it generated 82.53 µmol of H_2 and 40.74 µmol of O_2 over 2 h, as measured by gas chromatography (GC). The evolved gas volumes maintained a molar ratio close to the expected 2:1 (H_2:O_2), consistent with water splitting stoichiometry. The measured gas evolution also closely matched the theoretical values assuming 100% Faradaic efficiency, indicating high accuracy and minimal gas loss during the reaction (Supplementary Fig. 8). The IPCE at 1.23 V vs. RHE was measured over the 300–950 nm range in Fig. 2f. The integrated J_{ph} was 23.25 mA cm^{-2}, which closely matched the J_{ph} obtained from the LSV measurement under one-sun illumination (Supplementary Fig. 9). In comparison with the photovoltaic performance, the short-circuit current density was similar to the integrated J_{ph} of the photoanode, indicating that the light-harvesting efficiency was well maintained during the transition to the PEC configuration, with minimal optical or interfacial losses (Supplementary Fig. 10). In addition, the applied bias photon-to-current efficiency (ABPE) spectrum of the Ni/FM/PbS-QD photoanode exhibited a peak efficiency of 2.81% at 1.02 V vs. RHE, as shown in Supplementary Fig. 11.

To benchmark the performance of our photoanode, we compiled a comprehensive comparison of chalcogenide-based photoanodes reported from 2009 to date. As shown in Supplementary Table 1, the Ni/FM/PbS-QD photoanode achieves a J_{ph} of 18.6 mA cm^{-2} at 1.23 V vs. RHE without the use of a sacrificial agent. This performance is competitive with prior chalcogenide systems and is comparable to reported values for $BiVO_4$ and α-Fe_2O_3 photoanodes, which are commonly studied metal oxide-based candidates for PEC water splitting (Supplementary Tables 2–3). These results place the Ni/FM/PbS-QD architecture as an efficient and stable chalcogenide-based photoanode operating without a sacrificial agent. A detailed summary of the literature data used in the comparison is provided in Supplementary Tables 1–3.

Stability evaluation of PbS-QD-based photoelectrodes

To further evaluate the stability of the Ni/FM/PbS-QD photoanode, we first compared its performance in the presence and absence of S^{2-}/SO_3^{2-} sacrificial agents in 1.0 M NaOH (Supplementary Fig. 12). As

https://doi.org/10.1038/s41467-025-65987-3

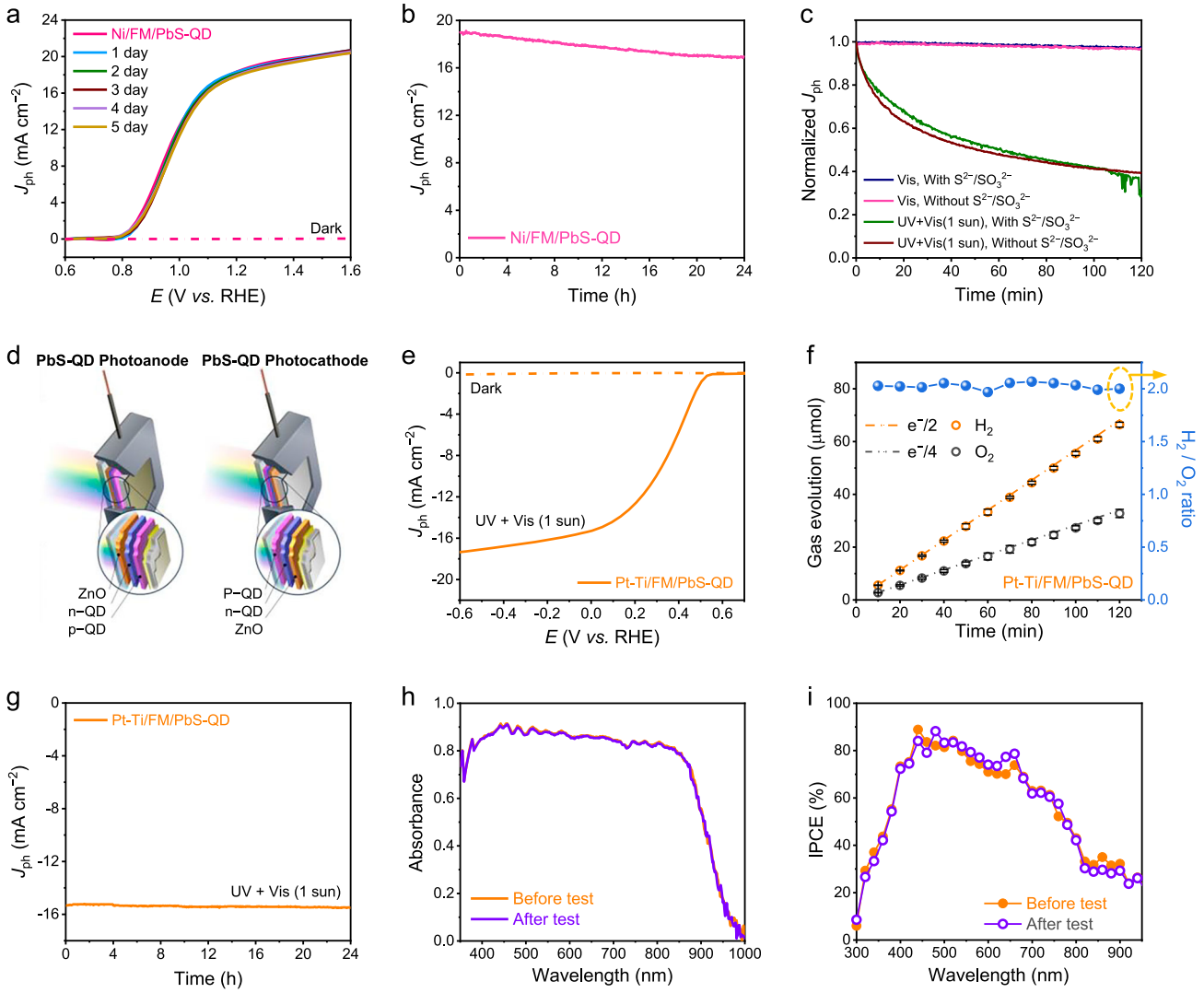

Fig. 4 | Comparison of PbS-QD-based photoelectrodes. a Chemical stability of the Ni/FM/PbS-QD photoanode, shown by linear sweep voltammetry (LSV) scans every 24 h over five consecutive days. The device was stored in 1.0 M sodium hydroxide (NaOH) in the dark and measured under visible-light illumination (λ ≥ 420 nm) at each time point. **b** Long-term stability test of the Ni/FM/PbS-QD photoanode for 24 h under visible-light illumination (λ ≥ 420 nm). **c** Normalized photocurrent density–time (J_{ph}–t) curves of the Ni/FM/PbS-QD photoanode with and without S^{2-}/SO_3^{2-} as a sacrificial agent, measured under visible-light illumination (λ ≥ 420 nm) and one-sun illumination (AM 1.5 G, 100 mW cm^{-2}). **d** Schematic illustration of the Ni/FM/PbS-QD photoanode and Pt-Ti/FM/PbS-QD photocathode. **e** LSV curve of Pt-Ti/FM/PbS-QD photocathode under one-sun illumination (AM 1.5 G, 100 mW cm^{-2}). **f** Time-resolved H_2 and O_2 production, along with the corresponding H_2/O_2 molar ratio indicated by the yellow arrow (right y axis, blue), from the Pt-Ti/FM/PbS-QD photocathode. Error bars represent the standard deviation from five independent measurements. **g** Long-term stability test of Pt-Ti/FM/PbS-QD photocathode for 24 h under one-sun illumination (AM 1.5 G, 100 mW cm^{-2}). **h** Ultraviolet–visible (UV–vis) spectra and **i**, incident photon-to-current efficiency (IPCE) data before and after long-term stability test for Pt-Ti/FM/PbS-QD photocathode.

shown in LSV measurements, the photoanode exhibited a J_{ph} of 19.06 mA cm^{-2} in the S^{2-}/SO_3^{2-} electrolyte, closely matching the value of 18.6 mA cm^{-2} in the sacrificial-agent-free NaOH solution. A cathodic shift in onset potential was observed in the presence of sacrificial agents, a well-established effect attributed to improved hole extraction and suppressed surface recombination. This shift indicates enhanced interfacial charge transfer dynamics rather than a significant increase in photocurrent. The chemical stability of the photoanode was further assessed by recording LSV curves over five consecutive days under visible-light illumination while the device was immersed in 1.0 M NaOH (Fig. 4a). The photocurrent remained nearly constant throughout the test period, confirming that the Ni and FM layers effectively passivate the PbS-QD surface. This passivation prevents water permeation and helps preserve the long-term performance of the photoanode. To assess operational durability, we conducted a continuous 24 h chronoamperometry test at 1.23 V vs. RHE under visible-light illumination. As shown in Fig. 4b, the J_{ph} decreased slightly from 18.6 to 16.9 mA cm^{-2}, indicating that the photoanode retained ~ 90% of its initial performance. To investigate potential surface changes on the Ni layer, X-ray photoelectron spectroscopy (XPS) was performed before and after the stability test. High-resolution Ni 2*p* spectra revealed characteristic peaks corresponding to Ni^{3+} and Ni^{2+} species, indicating partial surface oxidation in the alkaline electrolyte[35–37]. Notably, the binding energies of the Ni $2p_{3/2}$ and Ni $2p_{1/2}$ peaks remained unchanged, suggesting that the surface oxidation did not significantly alter the chemical state of the Ni layer (Supplementary Fig. 13). The effectiveness of surface passivation was further examined using depth-profiling XPS analysis of Ni/FM/PbS-QD photoanodes after chronoamperometric measurements conducted for 0 min (pristine), 10 min, 1 h, 24 h, 3 days, and 5 days (Supplementary Fig. 14). Before etching, the O 1*s* spectra exhibited distinct changes depending on the PEC operation time. However, after Ar^+ ion etching

(100 s per cycle, ~10 nm per cycle), the O 1*s* peaks of the pristine and 5-day samples appeared nearly identical. As shown in Supplementary Fig. 14e, the depth profiles of Ni 2*p* and O 1*s* atomic concentrations over 10 etching cycles revealed that Ni oxidation was largely confined to a thin surface layer. These results confirm minimal oxidation penetration and no evidence of electrolyte infiltration or structural degradation of the photoanode. In addition, the SEM and EDS analyses before and after the long-term stability test revealed no noticeable changes in surface morphology or elemental composition, confirming the structural and chemical stability of the Ni/FM passivation (Supplementary Fig. 15). To investigate in more detail, inductively coupled plasma-optical emission spectroscopy (ICP-OES) measurements were conducted to detect the leaching of Pb, S, or Ni during PEC H_2 production. Electrolyte samples were collected at various time intervals (0, 2, 6, 12, and 24 h), as shown in Supplementary Fig. 16. The analysis confirmed no significant presence of Ni ions, with no detectable leaching of Pb or S. Notably, negative values in ICP-OES indicate that the elements are either absent or below the detection limit owing to background correction and instrumental noise. These results suggest that the decrease in J_{ph} of the Ni/FM/PbS-QD photoanode is not primarily due to degradation of the PbS-QD layer or Ni catalyst. This observation is further supported by the Ni 2p XPS spectra, which remained unchanged before and after the stability test.

We further evaluated photostability under four conditions: with and without S^{2-}/SO_3^{2-}, and under visible-light and one-sun illumination. As shown in Fig. 4c, the Ni/FM/PbS-QD photoanode maintained stable photocurrent under visible-light illumination, with no significant degradation in either case. In contrast, under one-sun illumination, the photocurrent exhibited exponential decay over time, regardless of the presence of sacrificial agents, indicating that UV exposure accelerates degradation of the photoanode. This behaviour was consistently reflected in the IPCE measurements (Supplementary Fig. 17), which showed a similarly pronounced decrease in efficiency under one-sun illumination. Despite the identical passivation/encapsulation, a significant difference in IPCE was observed between one-sun and visible-light-only conditions, indicating that UV light plays a critical role in photoanode degradation. These results suggest that the reduced stability under one-sun conditions primarily arises from UV-induced damage, whereas under visible-light illumination, both the optical performance and structural stability of the photoanodes are largely preserved.

We hypothesise that this instability originates from UV-induced damage to the PbS-QD layer on the ZnO substrate. To explore this, we investigated the potential role of ZnO in facilitating UV-induced degradation. UV–vis absorption spectra of the PbS-QD/ZnO layer were recorded before and after continuous one-sun illumination. As shown in Supplementary Fig. 18, a significant decrease in the absorbance of the PbS-QD layer was observed after illumination, indicating degradation of the PbS-QD layer. This degradation is likely driven by surface oxidation of PbS-QD, potentially accelerated by adsorbed oxygen species on the ZnO surface under UV exposure[38]. Notably, similar degradation phenomena have been reported in PbS-QD photovoltaic devices that utilize ZnO as the electron-transport layer (ETL) on the front side exposed to UV light[39–41].

To investigate the role of ZnO in the UV-induced degradation of the PbS-QD layer, we modified the device architecture by repositioning the ZnO layer beneath the PbS-QD layer, thereby constructing a photocathode. This photocathode, denoted as Pt-Ti/FM/PbS-QD, employed a Pt-deposited Ti foil as the hydrogen evolution reaction (HER) catalyst (Fig. 4d). In this arrangement, the PbS-QD layers absorb incident UV light before it reaches the ZnO interface, mitigating direct UV exposure to the underlying ZnO. Before further evaluating PEC performance, we first confirmed the successful fabrication of the inverted-structure photocathode by conducting Mott–Schottky (MS) analysis, as shown in Supplementary Fig. 19. The MS plots exhibited a positive slope for the Ni/FM/PbS-QD photoanode and a negative slope for the Pt-Ti/FM/PbS-QD photocathode, confirming the n-type and p-type characteristics of the respective PbS-QD-based photoelectrodes. These results verify that the photocathode was successfully fabricated with the intended electronic properties. Notably, the flat-band potentials of both photoelectrodes, determined from the x-axis intercepts in the MS plots, are within approximately 0.15 V of the onset potentials observed in the LSV measurements of J_{ph}. This small potential difference suggests favourable interfacial energetics for efficient charge extraction. Moreover, this interpretation is supported by the enhanced τ_d observed in Supplementary Fig. 7, which is attributed to efficient charge separation and rapid interfacial electron-transfer kinetics, consistent with suppressed surface recombination. As shown in Fig. 4e, the Pt-Ti/FM/PbS-QD photocathode exhibited a J_{ph} of 15.35 mA cm^{-2} with an onset potential of 0.55 V vs. RHE under one-sun illumination. For the Pt-Ti/FM/PbS-QD photocathode, gas evolution was evaluated at 0 V vs. RHE over a 2-h period using GC, as shown in Fig. 4f. The experimentally measured gas volumes closely matched the theoretical values, with a H_2:O_2 molar ratio of approximately 2:1. Specifically, 66.41 µmol of H_2 and 32.77 µmol of O_2 were generated, corresponding to average Faradaic efficiency of 97.56% and 96.27%, respectively (Supplementary Fig. 20). To assess operational durability, long-term stability tests were conducted at 0 V vs. RHE for 24 h under one-sun illumination. As shown in Fig. 4g, the Pt-Ti/FM/PbS-QD photocathode showed improved operational photocurrent stability compared with the Ni/FM/PbS-QD photoanode under identical conditions without a UV filter. Furthermore, UV–vis absorption and IPCE spectra acquired before and after the 24-h test revealed no measurable changes, demonstrating the chemical stability and photostability of the photocathode (Fig. 4h, i). After the 24-h measurement, a long-term stability test lasting over 100 h was performed at 0 V vs. RHE to assess the durability of the photocathode (Supplementary Fig. 21a). To ensure consistent operation, the electrolyte was continuously stirred and purged with argon to prevent gas-bubble accumulation. The photocathode maintained consistent performance during the extended test, indicating negligible degradation. As shown in Supplementary Fig. 21b, ICP-OES analysis of the electrolyte after the stability test revealed no detectable leaching of other ions, except for a trace amount of Pt observed at the 2-h mark. Its concentration remained nearly unchanged thereafter, further confirming the structural integrity and chemical stability of the Pt-Ti/FM/PbS-QD photocathode. Moreover, SEM and EDS analyses were conducted to evaluate the stability of the Pt-Ti foil as a passivation layer. No significant changes were detected before and after the long-term stability test, confirming their structural and chemical robustness (Supplementary Fig. 22). To directly compare the PEC stability of the photoanode and photocathode architectures, we conducted 25 consecutive LSV scans under one-sun illumination, as shown in Supplementary Fig. 23. The Ni/FM/PbS-QD photoanode showed a gradual decline in J_{ph} across cycles, indicating photocorrosion likely driven by UV-induced degradation at the ZnO/PbS-QD interface. In contrast, the Pt-Ti/FM/PbS-QD photocathode maintained stable performance with negligible variation throughout the cycling test. Collectively, these results suggest that the reduced stability of the PbS-QD photoanode under one-sun illumination originates from UV-induced degradation of PbS-QD in direct contact with the ZnO layer. In contrast, reordering the layer structure to shield ZnO from incident UV light significantly improves photoelectrode stability. This approach demonstrates that both PbS-QD photoanodes and photocathodes can be conveniently fabricated by reversing the layer sequence, offering a versatile and modular strategy for photoelectrode design.

Discussion

In summary, we significantly enhanced the stability of the PbS-QD layer by introducing a metal-layer passivation strategy that effectively

inhibits electrolyte permeation and prevents interfacial degradation. This approach enabled the development of a stable and efficient PbS-QD-based photoelectrode capable of operating without a sacrificial reagent. The Ni/FM/PbS-QD photoanode achieved a J_{ph} of 18.6 mA cm^{-2} at 1.23 V vs. RHE, demonstrating performance competitive with previously reported chalcogenide-based photoelectrodes. Moreover, the device retained 90% of its initial performance over 24 h in 1.0 M NaOH, demonstrating durability under alkaline conditions. Mechanistic investigation revealed that the reduced stability observed under one-sun illumination originates from UV-induced degradation of the PbS-QD layer in contact with the ZnO electron-transport layer. By inverting the layer configuration to construct a photocathode, and thus shielding ZnO from direct UV exposure, we achieved substantially improved long-term stability. This finding underscores the critical influence of device architecture on operational robustness. Furthermore, we anticipate that replacing ZnO with a less UV-sensitive material, such as SnO_2, could further enhance photoanode stability. This work demonstrates a scalable and generalisable strategy for fabricating stable and efficient chalcogenide-based photoelectrodes without the need for sacrificial agents. The metal-passivation approach presented here may be readily extended to other quantum dot systems, including CdS and CdSe, offering broad utility for next-generation PEC water-splitting technologies.

Methods

Materials

The materials used in the experiments included lead(II) acetate trihydrate (99%, Alfa Aesar), oleic acid (technical grade, 90%, Sigma-Aldrich), 1-octadecene (technical grade, 90%, Alfa Aesar), hexamethyldisilathiane (synthesis grade, Sigma-Aldrich), toluene (anhydrous, 99.8%, Sigma-Aldrich), methanol (anhydrous, 99.8%, Sigma-Aldrich), octane (anhydrous, ≥99%, Sigma-Aldrich), N,N-dimethylformamide (DMF, anhydrous, 99.8%, Sigma-Aldrich), lead(II) iodide (PbI_2, 99.99%, trace metals basis, Tokyo Chemical Industry), lead(II) bromide ($PbBr_2$, ≥98%, Tokyo Chemical Industry), 2-propanol (IPA, anhydrous, 99.5%, Sigma-Aldrich), butylamine (99.5%, Sigma-Aldrich), 1,2-ethanedithiol (EDT, Sigma-Aldrich), and acetonitrile (anhydrous, 99.8%, Sigma-Aldrich). Ni foils (100 µm, 99.5% metals basis, Alfa Aesar) and Ti foils (250 µm, annealed, 99.5%, Alfa Aesar) were also used. Field's metal (FM), a eutectic alloy consisting of indium (51%), bismuth (32.5%), and tin (16.5%), was purchased from Alfa Aesar (USA).

Synthesis of PbS-QD

Oleic acid-capped PbS-QD were synthesised using a rapid hot injection method. In a three-necked flask, 8 mmol of lead acetate trihydrate and 7 mL of oleic acid were dissolved in 40 mL of 1-octadecene under vacuum conditions and heated at 90 °C for 2 h. Subsequently, 3.40 mmol of hexamethyldisilathiane mixed with 10 mL of 1-octadecene was prepared as the sulphur precursor. This mixture was rapidly injected into the reaction flask under nitrogen at 120 °C and maintained for approximately 5 s. Subsequently, the flask was transferred to a water bath and 20 mL of toluene was added. The QD were purified by precipitation using toluene/acetone and toluene/methanol mixtures, followed by drying under vacuum. The synthesised PbS-QD were finally dispersed in octane.

Preparation of n-QD ink

To prepare the *n*-QD ink, 5 mL of N,N-dimethylformamide (DMF), containing 0.5 mmol of PbI_2, 0.1 mmol of $PbBr_2$, and 0.2 mmol of ammonium acetate, was vigorously mixed with 5 mL of the PbS-QD solution in octane (10 mg/mL) at 35 °C. After 15 min, the PbS-QD were completely transferred to the DMF phase. The QD in the DMF solution was washed twice with octane and precipitated by adding approximately 2.7 mL of toluene. The solid QD was separated by centrifugation and dried in a vacuum oven for 15 min.

Solar cell characterization

The current density–voltage characteristics were measured in reverse-scan mode from 1.0 V to −0.05 V (step 42 mV; delay 0.04 s) using a Keithley 2401 SourceMeter. Illumination was provided by an AM 1.5 G one-sun solar simulator equipped with a xenon arc lamp (Newport LCS-100). All measurements were conducted in a nitrogen-filled glove box. External quantum efficiency (EQE) was measured using a Quant-2000 system with a monochromatic light source modulated at 10 Hz and a Si/Ge photodiode as the reference. EQE measurements were performed in a nitrogen-purged box under 10% relative humidity.

Fabrication of photoanodes for PEC water splitting

The indium tin oxide (ITO) substrate was cleaned by sonication in acetone and isopropyl alcohol for 20 min and dried at 120 °C overnight. A ZnO layer was spin-coated onto the ITO substrate at 1000 rpm for 20 s. The as-prepared *n*-QD solid was diluted with a 5% butylamine solution in dimethylformamide (~700 mg mL^{-1}). This n-QD ink solution was then spin-coated onto the ZnO film at 600 rpm for 80 s and heated at 100 °C for 1 min. Subsequently, a p-QD layer was fabricated on the n-QD light-absorbing layer to serve as a hole-transporting layer. Spin-coating of unexchanged PbS-QD in octane (45 mg mL^{-1}) was performed at 2000 rpm for 10 s, followed by coating with an EDT solution in acetonitrile (2 mM) at 2000 rpm for 3 s. Thereafter, the sample was washed twice with acetonitrile. Subsequently, a 70-nm-thick layer of Au was thermally evaporated as the anode under low pressures (<10^{-6} torr). Field's metal (comprising 51.0% In, 32.5% Bi, and 16.5% Sn, sourced from Rotometals, Inc.) and a Ni foil (purity: 99.5%; thickness: 100 µm; Alfa) were sonicated in deionised water, ethanol, and acetone for 20 min to remove any residues. To establish an ohmic contact, Field's metal was inserted between the Ni foil and Au layer and melted on a hotplate at 65 °C. An enamel-insulated copper wire was also connected to the ITO electrode using Field's metal. The entire PEC device was encapsulated with epoxy resin and cured overnight under ambient conditions. For the fabrication of the Spu-Ni/PbS-QD photoanode, a 100 nm-thick Ni film was deposited using a DC sputtering system (Model: SRN-120, SORONA). The system operates with a maximum output of 3 kW DC power supplied to the cathode, generating plasma to sputter Ni onto the substrate. Prior to deposition, the substrate underwent RF pre-cleaning at 300 W. The deposition was carried out at 400 °C (±3%), resulting in a uniform and strongly adherent Ni layer, which served as the Spu-Ni base for subsequent PbS-QD layer formation. The same epoxy encapsulation method was applied for this device.

Fabrication of photocathode for PEC water splitting

The Pt-Ti/FM/PbS-QD photocathode was fabricated by repositioning the ZnO layer beneath the PbS-QD layer. A 20 nm Pt layer was deposited on Ti foil via electron-beam evaporation and bonded to the structure using molten Field's metal (FM). The loading of Pt was estimated to be less than 1 µg cm^{-2}. The device was encapsulated with epoxy (J-B Weld, USA), and a copper wire was connected for electrical contact.

PEC measurements

The PbS-QD-based photoelectrodes were evaluated for solar hydrogen evolution in a three-electrode configuration using a saturated mercury/mercuric oxide (Hg/HgO) reference electrode (RE-61AP, ALS Co. Ltd.) and a Pt wire as the counter electrode. The active surface area of the photoelectrode used for all measurements was 0.2 cm^2, defined as the illuminated region exposed to the electrolyte during testing. The photoanode measurements were conducted in a stirred 1.0 M NaOH (98%, Alfa Aesar) electrolyte, which was bubbled with argon and illuminated under one-sun conditions with a UV cut-off filter (λ ≥ 420 nm). The measured potential ($V_{Hg/HgO}$) was

converted to the reversible hydrogen electrode (RHE) reference scale using the Nernst equation:

$$E\ (V\ vs.RHE) = E\ (V_{Hg/HgO}) + 0.059 \times pH + 0.098 \quad (1)$$

Incident photon-to-current efficiency (IPCE) data were recorded using a 300 W Xe arc lamp (66902, Newport) as the light source, equipped and a monochromator (CS260, Newport). The intensity of the reference light was calibrated before the IPCE measurement. The IPCE was calculated by following equation:

$$IPCE\ (\%) = \left(\frac{1240 \times J_{ph}}{\lambda \times P_{in}}\right) \times 100 \quad (2)$$

where J_{ph} is the photocurrent density (mA cm^{-2}), λ is the wavelength of incident light (nm) and P_{in} (mW cm^{-2}) is the incident light intensity.

For a photoanode, the applied bias photon-to-current efficiency (ABPE) is calculated using the following formula:

$$ABPE\ (\%) = \left(\frac{J_{ph} \times \left(1.23 - V_{app}\right)}{P_{in}}\right) \times 100 \quad (3)$$

where V_{app} is the applied potential vs. RHE (V), and 1.23 V is the thermodynamic potential required for water splitting. The ABPE value was calculated based on the optimal sample, and this measurement was performed once.

The resistance and capacitance values of the electrochemical cells were determined using an Ivium electrochemical workstation. The electrochemical impedance spectroscopy (EIS) measurements were conducted over the frequency range from 3 MHz to 0.5 Hz with an amplitude of 20 mV. The impedance spectra were fitted with an equivalent circuit model using ZView2 software, yielding parameters such as the series resistance, charge-transfer resistance, recombination resistance, and the corresponding capacitances. The measurements were performed once for the optimal sample of each electrode type, and the obtained resistance and capacitance values are reported in the text and in the captions of the relevant figures.

Intensity-modulated photocurrent spectroscopy (IMPS) was conducted over a frequency range from 10 kHz down to 0.1 Hz, using a light-emitting diode (LED, centre wavelength ≈ 740 nm) as the perturbation source. The modulation amplitude of the incident light was set to 10%. The electron transport time (τ_d) was obtained from the characteristic frequency at the minimum of the IMPS semicircle (f_{min}) according to

$$\tau_d = \frac{1}{2\pi f_{min}} \quad (4)$$

Mott–Schottky plots were recorded in the dark at a scan rate of 10 mV s^{-1} and a fixed frequency of 100 Hz. The acceptor density (N_A) was determined using:

$$\frac{1}{C^2} = \frac{2}{e_0 \varepsilon \varepsilon_0 N_A}\left(E - E_{fb} - \frac{k_B T}{e}\right) \quad (5)$$

where C is the space-charge capacitance, e is the elementary charge (1.602×10^{-19} C), ε is the relative dielectric constant of the perovskite (≈32.5)[42], ε_0 is the vacuum permittivity (8.854×10^{-12} F m^{-1}), respectively. E is the applied potential (V vs. RHE), E_{fb} is the flat-band potential (V vs. RHE), k_B is the Boltzmann constant (1.381×10^{-23} JK^{-1}), and T is the absolute temperature (in K).

Photoelectrochemical H_2 evolution test

Hydrogen evolution was monitored using Ar carrier gas and quantified by gas chromatography (6500GC, YL Instruments) every 10 min for 2 h at 1.23 V vs. RHE. Ar gas was supplied at 50 sccm via a mass flow controller (5850E, Brooks Instruments), and the reactor outlet was connected to the GC via a polytetrafluoroethylene (PTFE) line. A water filter (202234-B, Chromatography Research Supplies, USA) was placed upstream of the GC to remove moisture. Calibration was performed using a standard gas mixture in an Ar balance. The Faradaic efficiency (η_F) for hydrogen was calculated as follows:

$$\eta_F\ (\%) = \left(\frac{\text{Generated gas (mol)} \times n \times F}{Q}\right) \times 100 \quad (6)$$

Where n is the number of electrons required for gas evolution (2 for H_2, 4 for O_2), F is the Faraday constant (96,485 C mol^{-1}), and Q is the total charge passed (C).

Characterisation

A UV-vis spectrophotometer (UV-2600, Shimadzu) was utilised to assess the optical properties of n-QD films. PL measurements were conducted using a Horiba FL3-2iHR spectrometer connected to InGaAs detector arrays, employing 400 nm monochromatic light as the excitation source. Cross-sectional images of the device were obtained through field-emission scanning electron microscopy (FE-SEM, JEOL JSM-7610F). Transmission electron microscopy (TEM) was conducted using JEOL JEM-2100F. The size of PbS-QD was analysed through ImageJ software. Fluorescence lifetime imaging microscopy (FLIM) was performed with a scanning confocal microscope (MicroTime 200, Picoquant, Germany) using a 100 × oil-immersion objective. A single-mode pulsed diode laser (470 nm wavelength, approximately 30 ps pulse width, ~0.1 μW average power, and 0.5 MHz repetition rate) served as the excitation source. The emissions from the samples were collected using a dichroic mirror (490 DCXR, AHF) and a long-pass filter (HQ500lp, AHF). FLIM images, comprising 200 × 200 pixels, were captured using the time-tagged time-resolved data acquisition method, with an acquisition period of 2 ms per pixel. Optical modelling was conducted using the transfer matrix formalism (TMF) method, with source code developed by the McGehee group. The optical constants of n-QD and p-QD were determined from variable-angle spectroscopic ellipsometry (VASE, WizOptics, Inc.) measurements. The reported values were used to determine the optical constants of ITO, ZnO, and Au.

Data availability

Source data are provided with this paper.

References

1. Nozik, A. Photoelectrolysis of water using semiconducting TiO_2 crystals. *Nature* **257**, 383–386 (1975).
2. Boddy, P. Oxygen evolution on semiconducting TiO_2. *J. Electrochem. Soc.* **115**, 199 (1968).
3. Wrighton, M. S. et al. Strontium titanate photoelectrodes. Efficient photoassisted electrolysis of water at zero applied potential. *J. Am. Chem. Soc.* **98**, 2774–2779 (1976).
4. Gerischer, H. Electrochemical behavior of semiconductors under illumination. *J. Electrochem. Soc.* **113**, 1174 (1966).
5. Fujishima, A. & Honda, K. Electrochemical photolysis of water at a semiconductor electrode. *Nature* **238**, 37 (1972).
6. Zeng, X. et al. Highly dispersed TiO_2 nanocrystals and WO_3 nanorods on reduced graphene oxide: Z-scheme photocatalysis system for accelerated photocatalytic water disinfection. *Appl. Catal. B* **218**, 163–173 (2017).

7. John, R. A. et al. Atomically altered hematite for highly efficient perovskite tandem water-splitting devices. *ChemSusChem* **10**, 2449–2456 (2017).
8. Pan, J. B. et al. Activity and stability boosting of an oxygen-vacancy-rich $BiVO_4$ photoanode by NiFe-MOFs thin layer for water oxidation. *Angew. Chem. Int. Ed.* **133**, 1453–1460 (2021).
9. Gui, M.-S. & Zhang, W.-D. Preparation and modification of hierarchical nanostructured Bi_2WO_6 with high visible light-induced photocatalytic activity. *Nanotechnology* **22**, 265601 (2011).
10. Zheng, G., Wang, J., Li, H., Li, Y. & Hu, P. WO_3/Cu_2O heterojunction for the efficient photoelectrochemical property without external bias. *Appl. Catal. B* **265**, 118561 (2020).
11. He, B. et al. General and robust photothermal-heating-enabled high-efficiency photoelectrochemical water splitting. *Adv. Mater.* **33**, 2004406 (2021).
12. Zhang, Z., Nagashima, H. & Tachikawa, T. Ultra-narrow depletion layers in a hematite mesocrystal-based photoanode for boosting multihole water oxidation. *Angew. Chem. Int. Ed.* **132**, 9132–9139 (2020).
13. Hao, Z., Liu, Z., Li, Y., Ruan, M. & Guo, Z. Enhanced photoelectrochemical performance of 2D core–shell $WO_3/CuWO_4$ uniform heterojunction via in situ synthesis and modification of Co-Pi co-catalyst. *Int. J. Hydrog. Energy* **45**, 16550–16559 (2020).
14. Chen, H. M. et al. Quantum dot monolayer sensitized ZnO nanowire-array photoelectrodes: true efficiency for water splitting. *Angew. Chem. Int. Ed.* **49**, 5966–5969 (2010).
15. Walter, M. G. et al. Solar water splitting cells. *Chem. Rev.* **110**, 6446–6473 (2010).
16. McDonald, S. A. et al. Solution-processed PbS quantum dot infrared photodetectors and photovoltaics. *Nat. Mater.* **4**, 138–142 (2005).
17. Sun, W.-T. et al. CdS quantum dots sensitized TiO_2 nanotube-array photoelectrodes. *J. Am. Chem. Soc.* **130**, 1124–1125 (2008).
18. Dong, Z. et al. Construction of CdS/Ti–Nb–O composite photoanode with favorable optical absorption and charge transfer for dramatically boosted photoelectrochemical water splitting. *Int. J. Hydrog. Energy* **48**, 32371–32384 (2023).
19. Jin, L. et al. Near-infrared colloidal quantum dots for efficient and durable photoelectrochemical solar-driven hydrogen production. *Adv. Sci.* **3**, 1500345 (2016).
20. Seol, M., Jang, J.-W., Cho, S., Lee, J. S. & Yong, K. Highly efficient and stable cadmium chalcogenide quantum dot/ZnO nanowires for photoelectrochemical hydrogen generation. *Chem. Mater.* **25**, 184–189 (2013).
21. Lim, C. et al. Effect of bandgap variation on photovoltaic properties of lead sulfide quantum dot solar cell. *Mater. Today Energy* **36**, 101357 (2023).
22. Chuang, C.-H. M., Brown, P. R., Bulović, V. & Bawendi, M. G. Improved performance and stability in quantum dot solar cells through band alignment engineering. *Nat. Mater.* **13**, 796–801 (2014).
23. Ma, Y. et al. Titanium dioxide-based nanomaterials for photocatalytic fuel generations. *Chem. Rev.* **114**, 9987–10043 (2014).
24. Schneider, J. & Bahnemann, D. W. Undesired role of sacrificial reagents in photocatalysis. *J. Phys. Chem. Lett.* **4**, 3479–3483 (2013).
25. Sheng, W. et al. Quantum dot-sensitized hierarchical micro/nanowire architecture for photoelectrochemical water splitting. *ACS Nano* **8**, 7163–7169 (2014).
26. Ghosh, D., Ghosh, A., Ali, M. Y. & Bhattacharyya, S. Photoactive core–shell nanorods as bifunctional electrodes for boosting the performance of quantum dot sensitized solar cells and photoelectrochemical cells. *Chem. Mater.* **30**, 6071–6081 (2018).
27. Wang, J.-C. et al. Highly efficient flexible inverted organic solar cells using atomic layer deposited ZnO as electron selective layer. *J. Mater. Chem.* **20**, 862 (2010).
28. Tokunaga, S., Kato, H. & Kudo, A. Selective preparation of monoclinic and tetragonal BiVO 4 with scheelite structure and their photocatalytic properties. *Chem. Mater.* **13**, 4624–4628 (2001).
29. Kudo, A., Omori, K. & Kato, H. A novel aqueous process for preparation of crystal form-controlled and highly crystalline $BiVO_4$ powder from layered vanadates at room temperature and its photocatalytic and photophysical properties. *J. Am. Chem. Soc.* **121**, 11459–11467 (1999).
30. Li, C., Hu, P., Meng, H. & Jiang, Z. Role of sulfites in the water splitting reaction. *J. Solut. Chem.* **45**, 67–80 (2016).
31. Mubarok, M. A. et al. Molecular engineering in hole transport π-conjugated polymers to enable high efficiency colloidal quantum dot solar cells. *Adv. Energy Mater.* **10**, 1902933 (2020).
32. Aqoma, H. et al. High-efficiency photovoltaic devices using trap-controlled quantum-dot ink prepared via phase-transfer exchange. *Adv. Mater.* **29**, 1605756 (2017).
33. Hyun, B.-R. et al. Electron injection from colloidal PbS quantum dots into titanium dioxide nanoparticles. *ACS Nano* **2**, 2206–2212 (2008).
34. Moreels, I. et al. Size-dependent optical properties of colloidal PbS quantum dots. *ACS Nano* **3**, 3023–3030 (2009).
35. Gao, M. et al. Efficient water oxidation using nanostructured α-nickel-hydroxide as an electrocatalyst. *J. Am. Chem. Soc.* **136**, 7077–7084 (2014).
36. Kenney, M. J. et al. High-performance silicon photoanodes passivated with ultrathin nickel films for water oxidation. *Science* **342**, 836–840 (2013).
37. Zheng, X. et al. Theory-driven design of high-valence metal sites for water oxidation confirmed using in situ soft X-ray absorption. *Nat. Chem.* **10**, 149–154 (2018).
38. Liu, C., Bi, Q., Leyland, A. & Matthews, A. An electrochemical impedance spectroscopy study of the corrosion behaviour of PVD coated steels in 0.5 N NaCl aqueous solution: Part II: EIS interpretation of corrosion behaviour. *Corros. Sci.* **45**, 1257–1273 (2003).
39. Wang, Y. et al. Hybrid thin film encapsulation for improving the stability of PbS quantum dot solar cells. *Small* **20**, 2404984 (2024).
40. Dastjerdi, H. T., Prochowicz, D., Yadav, P. & Tavakoli, M. M. Luminescence down-shifting enables UV-stable and efficient ZnO nanowire-based PbS quantum dot solar cells with J_{sc} exceeding 33 mA cm^{-2}. *Sustain. Energy Fuels* **3**, 3128–3134 (2019).
41. Kirmani, A. R. et al. Colloidal quantum dot photovoltaics using ultrathin, solution-processed bilayer In_2O_3/ZnO electron transport layers with improved stability. *ACS Appl. Energy Mater.* **3**, 5135–5141 (2020).
42. Xia, J. et al. Deep surface passivation for efficient and hydrophobic perovskite solar cells. *J. Mater. Chem. A* **9**, 2919–2927 (2021).

Acknowledgements

This research was supported by the National Research Foundation (RS-2024-00456139, RS-2023-00222006, and 2022R1I1A1A01064236), and by the Basic Science Research Programme through the National Research Foundation of Korea (NRF) funded by the Ministry of Education. This work was also supported by the InnoCORE programme of the Ministry of Science and ICT(1.250022).

Author contributions

H.-Y. Y., M. A. M., S. K., and S.-H. L. conceived and proposed the project under the supervision of S.-Y. J. and J.-W. J. M. A. M., and S.-H. L. prepared and characterized the PbS-QD solar cells. H.-Y. Y., and S. K. prepared and characterized the PbS-QD photoelectrodes with the assistance of J. M. Y., J. Jo., and A. T. H.-Y. Y., M. A. M., S. K., S.-H. L., S.-Y. J., and J.-W. J. co-wrote the manuscript.

Competing interests

The authors declare no competing interests.

Additional information

Supplementary information The online version contains supplementary material available at https://doi.org/10.1038/s41467-025-65987-3.

Correspondence and requests for materials should be addressed to Sung-Yeon Jang or Ji-Wook Jang.

Peer review information *Nature Communications* thanks Su-Il In, Xin Tong, Xuhui Sun, and the other anonymous reviewer(s) for their contribution to the peer review of this work. A peer review file is available.